

# High-Frequency Semantics and Geometric Priors for End-to-End Detection Transformers in Challenging UAV Imagery

Hongxing Peng<sup>a</sup>, Lide Chen<sup>a</sup>, Hui Zhu<sup>b</sup> and Yan Chen<sup>a,\*</sup>

<sup>a</sup>College of Mathematics and Informatics, South China Agricultural University, Guangzhou 510642, China

<sup>b</sup>Key Laboratory of Smart Agricultural Technology in Tropical South China, Ministry of Agriculture and Rural Affairs, Guangzhou 510642, China

<sup>c</sup>School of Economics and Trade, Guangdong Mechanical & Electrical Polytechnic, Guangzhou 510545, China

## ARTICLE INFO

### Keywords:

Unmanned Aerial Vehicle  
Small object detection  
Detection Transformer  
Real-time

## ABSTRACT

Unmanned Aerial Vehicle-based Object Detection (UAV-OD) faces substantial challenges, including small target sizes, high-density distributions, and cluttered backgrounds in UAV imagery. Current algorithms often depend on hand-crafted components like anchor boxes, which demand fine-tuning and exhibit limited generalization, and Non-Maximum Suppression (NMS), which is threshold-sensitive and prone to misclassifying dense objects. These generic architectures thus struggle to adapt to aerial imaging characteristics, resulting in performance limitations. Moreover, emerging end-to-end frameworks have yet to effectively mitigate these aerial-specific challenges. To address these issues, we propose HEGS-DETR, a comprehensively enhanced, real-time Detection Transformer framework tailored for UAVs. First, we introduce the High-Frequency Enhanced Semantics Network (HFESNet) as a novel backbone. HFESNet preserves critical high-frequency spatial details to extract robust semantic features, thereby improving discriminative capability for small and occluded targets in complex backgrounds. Second, our Efficient Small Object Pyramid (ESOP) strategy strategically fuses high-resolution feature maps with minimal computational overhead, significantly boosting small object detection. Finally, the proposed Selective Query Recollection (SQR) and Geometry-Aware Positional Encoding (GAPE) modules enhance the detector's decoder stability and localization accuracy, effectively optimizing bounding boxes and providing explicit spatial priors for dense scenes. Experiments on the VisDrone dataset demonstrate that HEGS-DETR achieves a 5.1% AP<sub>50</sub> and 3.8% AP increase over the baseline, while maintaining real-time speed and reducing parameter count by 4M.

## 1. Introduction

Real-time object detection on Unmanned Aerial Vehicles (UAVs) has emerged as a cornerstone technology, underpinning a multitude of critical applications ranging from precision agriculture [30] and highway surveillance [34] to urban environmental assessment [9]. However, the unique vantage point of aerial imagery presents a confluence of complex challenges that push the performance of existing detection models to their limits. Models must contend with high-density scenes populated with numerous small objects and frequent occlusions caused by cluttered backgrounds, all while operating under the stringent constraints of limited on-board computational resources and the demand for real-time processing [26].

Prevailing UAV object detection models [32, 36, 8, 19] rely on predefined anchor boxes and Non-Maximum Suppression (NMS), which introduce inherent limitations. Anchor box parameters require meticulous tuning for specific datasets and lack generalization capability. Meanwhile, NMS is sensitive to its threshold, potentially leading to the erroneous suppression of highly overlapping or adjacent objects or the failure to remove redundant detections. These

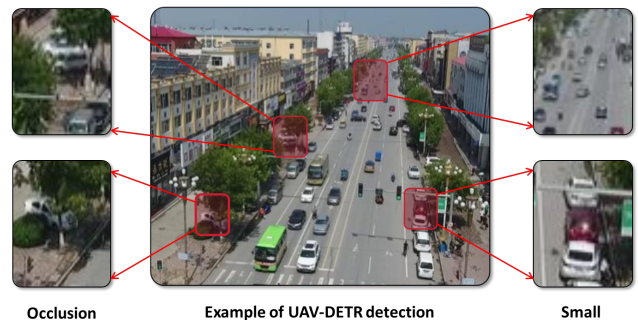


**Figure 1:** Challenges in UAV Object Detection: dense small objects and cluttered backgrounds

issues create significant processing bottlenecks, particularly in the dense-object scenarios common in UAV footage.

The advent of the Detection Transformer (DETR) [2] marked a paradigm shift towards truly end-to-end, NMS-free detection, though its substantial computational overhead initially rendered it impractical for real-time applications. A major breakthrough arrived with RT-DETR [33], the first end-to-end framework to surpass state-of-the-art YOLO models under real-time conditions. Its advantage is credited to an innovative hybrid encoder design that decouples intra-scale feature interaction from cross-scale feature fusion.

Despite RT-DETR's impressive performance on general-purpose benchmarks such as COCO [15], its architecture is not inherently optimized for the distinct challenges of aerial

\*Corresponding author

✉ xyphx@scau.edu.cn (H. Peng); 20243170009@stu.scau.edu.cn (L. Chen); zhuohui@gdmeec.edu.cn (H. Zhu); chenyscau@scau.edu.cn (Y. Chen)  
ORCID(s): 0000-0002-1872-8855 (H. Peng); 0009-0009-3953-1689 (L. Chen)

imagery—namely, small target sizes, high object density, and frequent occlusions, as illustrated in fig. 1. Its feature extractor and decoder were not purpose-built to address these core problems endemic to the aerial domain. Consequently, while RT-DETR provides a powerful baseline, unlocking its full potential for aerial object detection necessitates a targeted redesign of its core components.

To address these challenges, we propose a novel framework built upon RT-DETR that integrates several synergistic innovations. First, to remedy the inadequate feature representation of standard networks for complex aerial scenes, we replace the conventional backbone with a High-Frequency Enhanced Semantics Network (HFESNet). This network is meticulously engineered to preserve fine-grained, high frequency details, thereby enriching the robust semantic context of deep features. These details are crucial for distinguishing objects with significant scale variation, overlapping, and occluded objects in higher-level layers.

Second, to overcome the irreversible loss of spatial information for diminutive objects caused by aggressive downsampling in standard models, we introduce an Efficient Small Object Pyramid (ESOP). This novel feature pyramid explicitly rescues and integrates high-resolution S2 feature maps into the multi-scale fusion process in a computationally efficient manner.

Finally, to bolster the decoder’s localization capabilities in dense scenes, we introduce a two-pronged strategy: a Selective Query Recollection (SQR) training mechanism, which mitigates cascading errors by providing stronger supervision to later decoding stages to address training instability caused by complex and ambiguous backgrounds; and a Geometry-aware Position Encoding (GAPE) strategy, which creates explicit spatial priors to guide the precise localization of tightly clustered targets.

Our main contributions are summarized as follows:

- 1) We propose the High-Frequency Enhanced Semantics Network (HFESNet), a novel backbone that optimally balances the preservation of high-frequency spatial details with the extraction of high-level semantic information, yielding more discriminative features for dense and cluttered aerial scenes.
- 2) We introduce the Efficient Small Object Pyramid (ESOP), a multi-scale fusion neck that strategically integrates high-resolution features (S2) via a lightweight pre-fusion module. This design significantly boosts small-object detection performance at a modest computational cost.
- 3) We enhance the decoder’s stability and localization accuracy through two key innovations: the Selective Query Recollection (SQR) training strategy stabilizes bounding box optimization by mitigating error accumulation, while the Geometry-aware Position Encoding (GAPE) module provides the decoder with rich spatial priors, markedly improving localization precision for dense and small objects.

- 4) Collectively, our proposed enhancements enable our model to significantly outperform the baseline RT-DETR on the challenging VisDrone aerial detection dataset [35]. While maintaining the real-time performance of RT-DETR, our model achieves a 5.1-point increase in AP<sub>50</sub> and a 3.8-point increase in AP, with a 4M reduction in parameters, thereby validating the efficacy of our targeted architectural redesign.

## 2. Relation Work

### 2.1. Real-time Object Detection on UAVs

Real-time object detection on Unmanned Aerial Vehicles (UAV-OD) is challenged by the detection of dense small objects and the handling of occlusions, compounded by stringent constraints on computational resources and real-time performance [26]. The field of real-time object detection has long been dominated by the YOLO family of models [32, 36, 8, 19], which established a high-performance benchmark for the trade-off between speed and accuracy. However, YOLO’s inherent dependence on a hand-crafted Non-Maximum Suppression (NMS) post-processing stage induces hyperparameter sensitivity and processing latency, a limitation that becomes a critical bottleneck in the dense-object scenarios characteristic of aerial viewpoints.

The introduction of the Detection Transformer (DETR) [2] signaled a paradigm shift toward truly end-to-end, NMS-free detection, though its substantial computational cost initially precluded its use in real-time applications. RT-DETR [33] represents a significant breakthrough as the first framework to achieve real-time end-to-end performance, even surpassing state-of-the-art YOLO models. This achievement is attributed to its innovative hybrid encoder, which decouples intra-scale feature interaction from cross-scale feature fusion.

Despite RT-DETR’s exceptional performance on general-purpose datasets such as COCO [15], its architecture is not inherently optimized for the unique challenges of aerial imagery. Its feature extractor and decoder were not designed to address the core issues intrinsic to UAV perspectives, namely, small target sizes, high target density, and frequent occlusions. Consequently, while RT-DETR provides a powerful baseline, unlocking its full potential in aerial detection necessitates a targeted redesign of its core components.

### 2.2. Semantic Enhancement with Frequency Awareness

To achieve effective object discrimination in complex aerial scenes, feature representations must simultaneously encapsulate rich semantic information and precise spatial details. While existing modules, such as the Feature Guided Enhancement (FGE) proposed by Huang et al. [11] to bolster small object features and the Cross-Stage Partial Context Transformer (CSP-COT) by Gao et al. [7] to capture global contextual relationships, can effectively recalibrate feature responses to emphasize salient information, they often do so at the expense of suppressing high-frequency spatial

details. This includes sharp edges and fine textures, which are essential for differentiating subtle, overlapping objects against cluttered backgrounds.

This trade-off is particularly detrimental in UAV Object Detection (UAV-OD), where a significant portion of the critical discriminative information is embedded within these high-frequency components. A backbone network that exclusively prioritizes the extraction of high-level semantic information will invariably obscure or discard these crucial details, leading to missed detections and inaccurate localization.

To address this dichotomy, we propose the High-Frequency Enhanced Semantics Network (HFESNet). Our backbone is specifically engineered to address the challenges of aerial detection, centered on the core principle of fusing fine-grained, high-frequency information from shallow layers with the robust semantic context constructed in deeper layers. This dual focus ensures the resulting feature maps retain high discriminability, enabling the model to effectively disambiguate occluded and densely packed objects.

### 2.3. Efficient Multi-scale Feature Fusion

The fundamental challenge in detecting small objects from an aerial perspective lies in preserving high-resolution spatial information. Multi-scale feature fusion, a concept pioneered by the Feature Pyramid Network (FPN) [14] and subsequently advanced in works such as PANet [16] and BiFPN [24], is the standard approach to address this issue. However, these architectures typically compromise on the highest resolution features to maintain computational efficiency. RT-DETR inherits this design philosophy; its feature pyramid is constructed using features from stages S3 through S5, effectively discarding the highest-resolution S2 feature map. This aggressive downsampling results in an irreversible loss of the fine-grained spatial information most critical for detecting minute objects. This informational deficit constitutes a core limitation in the direct application of standard RT-DETR to aerial scenarios.

To fill this specific gap, we introduce the Efficient Small Object Pyramid (ESOP). Our approach modifies the RT-DETR encoder to explicitly rescue and integrate the high-resolution S2 feature map into the multi-scale fusion process. By means of a lightweight downsampling and pre-fusion module, ESOP efficiently incorporates the fine-grained details necessary for enhancing small object detection into the feature pyramid, all while preserving the real-time processing capabilities of the original architecture.

### 2.4. Mitigating Cascading Errors in Decoders

A recognized challenge in cascaded decoder architectures is error accumulation [22]. Specifically, prediction deviations generated in the early stages of the decoding process propagate to subsequent stages, impeding the fine-grained refinement of bounding boxes. This problem is particularly exacerbated in Unmanned Aerial Vehicle (UAV) imagery, where complex and ambiguous backgrounds can easily destabilize the training process. To counteract this issue, research has explored enhancing decoder performance

by improving query refinement mechanisms. For instance, the work on SQR-DETR [3] demonstrated that passing well-initialized queries from lower-level decoder stages to higher ones provides a stronger supervisory signal, effectively mitigating such cascading errors.

In light of this, we devise a Selective Query Recollection (SQR) training strategy tailored for the RT-DETR-R18 architecture. Diverging from the baseline model, our approach selectively re-introduces high-quality queries from lower-level decoder outputs during the training phase. This mechanism furnishes the higher decoder layers with a stronger supervisory signal, thereby stabilizing the bounding box refinement process and effectively preventing the degradation of prediction quality in deeper stages. This is critical for robustly handling complex aerial scenes.

### 2.5. Enhancing Spatial Priors for Precise Localization in Decoders

Beyond achieving stable optimization, the precise spatial localization of small, densely distributed objects requires the decoder to be guided by rich spatial prior information. However, the standard RT-DETR decoder generates positional encodings via a simplistic mechanism: a mere linear projection of its reference points. This approach provides insufficient spatial constraints, rendering it difficult to effectively distinguish between adjacent targets separated by only a few pixels. Although prior works such as PETR [17] and Conditional DETR [18] have demonstrated significant performance gains from incorporating geometric or conditional spatial information, constructing an efficient yet explicit spatial prior for real-time aerial detection remains a critical, unresolved challenge.

To address this gap, we propose the Geometry-aware Position Encoding (GAPE). The essence of this method lies in moving beyond the conventional linear projection to instead construct an explicit spatial prior. Its core innovation is the fusion of two key information types: the relative offsets of the Object Queries and the absolute coordinate information embedded in the sinusoidal positional encodings of the reference points. This fused positional information provides the decoder with a more lucid and profound understanding of fine-grained spatial relationships, thereby significantly enhancing the localization accuracy for the highly dense and minute targets prevalent in UAV-based visual scenes.

## 3. Methodologies

As illustrated in fig. 2, this study proposes HEGS-DETR based on the RT-DETR-R18 architecture [33]. We enhance the model through four critical components/strategies. First, we develop HEFSNet to replace the original backbone network, which facilitates discriminative feature learning for improved object separability under scenarios with dense small targets and complex backgrounds. Second, we propose the ESOP strategy to balance model complexity while effectively enhancing small object detection performance. Third, we introduce the GAPE strategy to construct explicit spatial priors that strengthen the model's capability

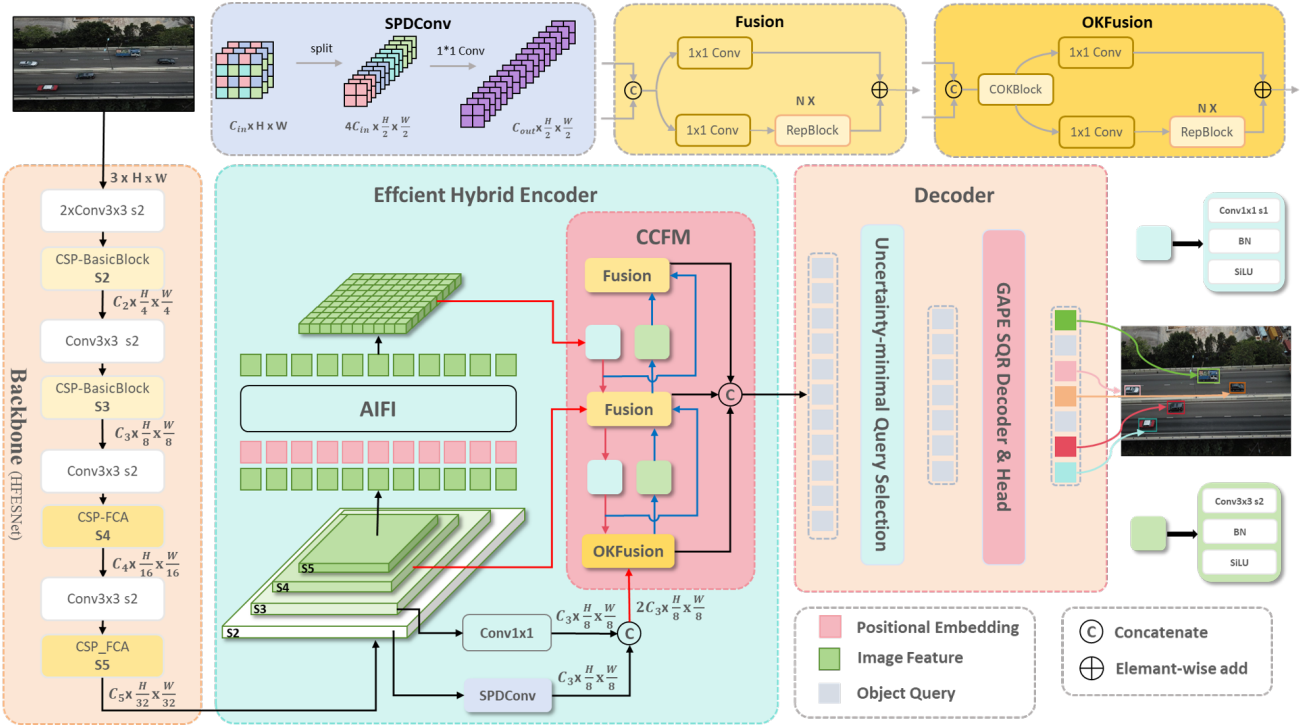


Figure 2: Overview of HEDS-DETR.

for precise localization. Finally, we design the SQR training strategy to stabilize bounding box optimization by shifting the training focus backward and alleviating decoder-induced error accumulation.

### 3.1. High-Frequency Enhanced Semantics Network

Advanced semantic features play a crucial role in enhancing target discriminability within the Attention-based Intra-scale Feature Interaction (AIFI) [33] module's self attention mechanism, which is particularly essential in scenes with dense small targets and complex backgrounds. However, deep features from traditional backbone networks, while possessing large receptive fields and rich semantic information, often suffer from the loss of high-frequency detail information.

To address this issue, we propose the High-Frequency Enhanced Semantics Network (HFESNet) as a replacement for the original ResNet-18 architecture. We developed the CSP-FCA module to replace two BasicBlocks in the deeper layers of ResNet-18, where the Frequency-aware Cascade Attention (FCA) [5] module integrates spatial, channel, and frequency information to recover high-frequency details. This module, combined with the Cross Stage Partial (CSP) [28] design philosophy, maintains deep semantic expressiveness while optimizing gradient propagation paths. Additionally, we designed the CSP-BasicBlock module to improve the first two layers of BasicBlocks in ResNet-18, further enhancing model expressiveness while reducing computational overhead.

As illustrated in fig. 2, given an input  $X$ , the CSP-FCA module first applies a  $1 \times 1$  convolution for preliminary channel-dimension transformation, yielding intermediate features  $X'$ . Subsequently,  $X'$  is divided along the channel dimension into two branches  $X'_1$  and  $X'_2$ , each containing half of the original number of channels. Branch  $X'_1$  directly preserves partial information from the original feature branch, while  $X'_2$  is processed by FCA to recover deep high-frequency information. These branches are then concatenated along the channel dimension and processed through another  $1 \times 1$  convolution to generate the module's output  $Y$ . The complete CSP-FCA pipeline can be formulated as:

$$\mathbf{X}' = \text{Conv}_{1 \times 1}(\mathbf{X}) \in \mathbb{R}^{H \times W \times C}, \quad (1)$$

$$\mathbf{X}' \xrightarrow{\text{channel split}} \begin{cases} \mathbf{X}'_1 \in \mathbb{R}^{H \times W \times \frac{C}{2}}, \\ \mathbf{X}'_2 \in \mathbb{R}^{H \times W \times \frac{C}{2}}, \end{cases} \quad (2)$$

$$\mathbf{Y} = \text{Conv}_{1 \times 1}(\text{Concat}(\mathbf{X}'_1, \mathcal{F}_{\text{FCA}}(\mathbf{X}'_2))). \quad (3)$$

As shown in fig. 3, The FCA module replaces the self attention mechanism and feed-forward network in the Transformer encoder, introducing Spatial Frequency Attention (SFA) and Dual Frequency Fusion Feed-Forward Network (DFFN). The SFA receives input features and generates query, key, and value vectors through linear layers for spatial self attention computation while simultaneously extracting channel features. SFA employs three projection operators: Spatial Projection (SP), Frequency Projection (FP),

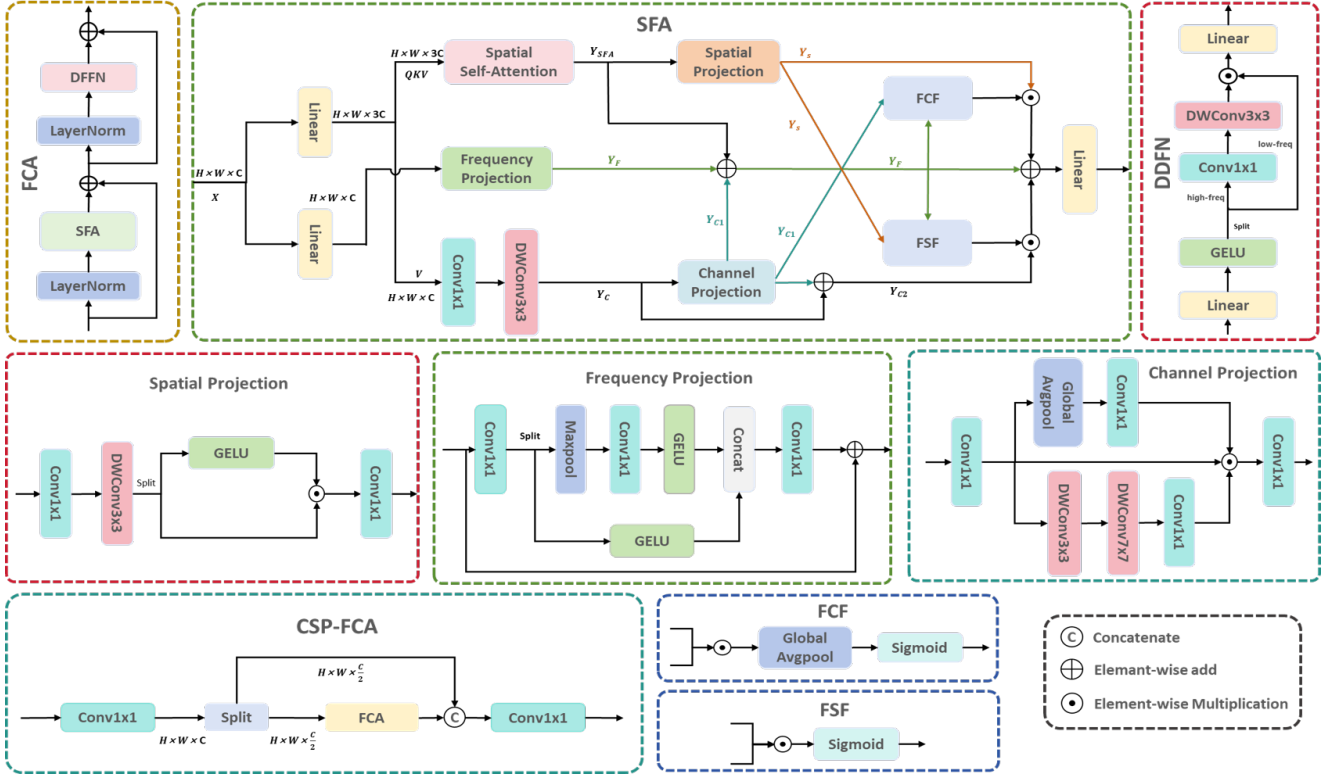


**Figure 3:** Illustrates the CSP-FCA module, which integrates the CSP strategy with the FCA (Feature Channel Attention) module.

and Channel Projection (CP) to extract features from different dimensions, which are subsequently integrated through Frequency-Channel Fusion (FCF) and Frequency-Spatial Fusion (FSF) for cross-branch weighted fusion. The DDFN further integrates low-frequency information from Transformers and high-frequency information from CNNs by separating input features into low-frequency and high-frequency components, enhancing the high-frequency portion before fusing it with low-frequency information.

The overall FCA process can be described as first applying SFA to process the input to obtain intermediate features, then utilizing DDFN to generate the final output. Both intermediate features and final outputs employ residual connections to preserve original information. This structure effectively retains low-frequency semantic representations while further enhancing high-frequency detail information:

$$X_{SFA} = \text{SFA}(\text{LayerNorm}(X_{in})) \oplus X_{in} \quad (4)$$

$$X_{out} = \text{DDFN}(\text{LayerNorm}(X_{SFA})) \oplus X_{SFA} \quad (5)$$

where  $X_{SFA}$  represents the output of the SFA module,  $\oplus$  denotes element-wise addition, and  $X_{out}$  denotes the final output of the FCA module.

### 3.2. Efficient Small Object Pyramid

RT-DETR uses feature maps from the last three stages for object detection. Due to multiple downsampling operations, these layers have lower spatial resolution, making it difficult to retain sufficient detail information and resulting in

inadequate detection performance for small objects. Lower layers possess higher resolution and richer local features; incorporating them can effectively compensate for the limitations of deep features in small object recognition and improve detection accuracy on small object datasets. However, this introduces issues such as increased computational complexity and processing time. To address this problem, as shown in fig. 2, we propose the Efficient Small Object Pyramid (ESOP) strategy, which uses SPDCConv downsampling to obtain information rich in small object details, then improves upon the Fusion module [33] to develop the OKFusion module with feature pre-fusion capabilities for comprehensive integration of cross-scale features with significant semantic differences. This efficiently enhances small object detection performance. The implementation details are as follows:

Since stride convolutions lose many critical details for small object detection, our model replaces stride convolutions with SPDCConv [23] when processing feature map  $S_2$ , dividing it into four sub-blocks before concatenation and adjusting channel dimensions with  $1 \times 1$  convolution, effectively preserving the fine-grained information necessary for small object detection. Simultaneously,  $S_3$  undergoes  $1 \times 1$  convolution transformation, and both are concatenated to obtain  $S_{23}$ . After  $S_5$  is processed by the AIFI module, it is fused with  $S_4$  through the Fusion module and transformed to obtain  $S_{45}$ . Previously, we had not performed feature fusion on  $S_{23}$ . Directly applying traditional RepConv [33] to  $S_{23}$  and  $S_{45}$  using the Fusion module might generate redundancy

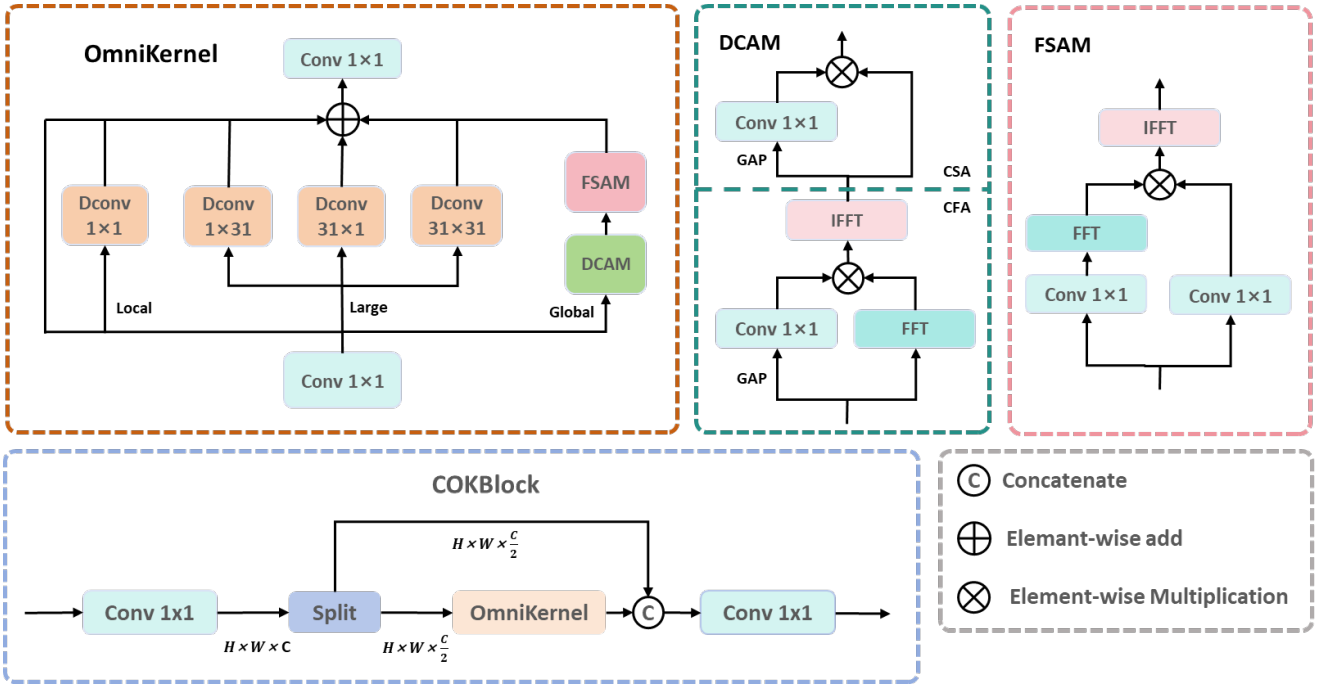


**Figure 4:** Illustrates the COKBlock, where FFT and IFFT denote the Fourier transform and inverse Fourier transform, respectively, and GAP denotes global average pooling.

or conflicts due to the direct mixing of information from different scales and semantic hierarchies. To solve this problem, we propose the OKFusion module: first concatenating  $S_{23}$  and  $S_{45}$  and inputting them into the COKBlock, then processing through convolution and RepBlock to obtain the fused feature  $S_{2345}$ , specifically:

$$S_{23} = \text{Concat}(\text{SPDCConv}(S_2), \text{Conv}(S_3)) \quad (6)$$

$$S' = \text{COKBlock}(\text{Concat}(S_{23}, S_{45})) \quad (7)$$

$$S_{2345} = \text{Conv}(S') \oplus \text{RepBlock}(\text{Conv}(S')) \quad (8)$$

Where  $S'$  represents an intermediate variable. As shown in fig. 4, The COKBlock is designed based on CSP architecture and the OmniKernel module [4], with the latter comprising three branches: local, large, and global. The large branch employs  $31 \times 31$  depth convolution and strip-shaped depth convolutions ( $1 \times 31$ ,  $31 \times 1$ ) to model long-distance dependencies. The global branch includes a dual-domain channel attention module (DCAM) [4] and frequency space attention module (FSAM) [4], focusing on information-rich frequency components through Fourier transformation and optimizing global features in the frequency domain. The local branch utilizes  $1 \times 1$  depth-separable convolution to modulate local signals, achieving multi-scale feature representation. COKBlock effectively learns feature representations from global to local while maintaining computational efficiency for feature map fusion. Given  $X$  processed by  $1 \times 1$  convolution to obtain  $X_{in}$ , the OmniKernel module is specifically represented as follows:

$$X_{Local} = \text{DConv}_{1 \times 1}(X_{in}) \quad (9)$$

$$X_{Large} = \text{DConv}_{1 \times 31}(X_{in}) + \text{DConv}_{31 \times 1}(X_{in}) + \text{DConv}_{31 \times 31}(X_{in}) \quad (10)$$

$$X_{Global} = \text{FSAM}(\text{DCAM}(X_{in})) \quad (11)$$

$$X_{out} = X_{in} + X_{Local} + X_{Large} + X_{Global} \quad (12)$$

Where DConv represents depth convolution, and  $X_{Local}$ ,  $X_{Large}$ , and  $X_{Global}$  are the outputs from the local, large, and global branches, respectively. The output of the OmniKernel module is obtained by processing  $X_{out}$  through a  $1 \times 1$  convolution.

### 3.3. Geometry-Aware Position Encoding

RT-DETR employs sinusoidal positional encoding in its Efficient Hybrid Encoder to preserve absolute spatial relationships. However, the positional encoding strategy for decoder queries relies on simple linear projection of reference point coordinates. This linear mapping may be insufficient to capture the geometric relationships between object queries and multi-scale image features obtained from the encoder output, thereby limiting the model's capability to precisely localize objects in complex scenarios involving small objects or dense targets. To address this limitation, we propose the Geometry-Aware Positional Encoding (GAPE) method, which first integrates the offset information of Object Queries with the absolute spatial information of Reference Points to construct explicit spatial priors, and then injects them into both the self-attention and cross-attention layers of the decoder, respectively. The specific implementation is as follows:

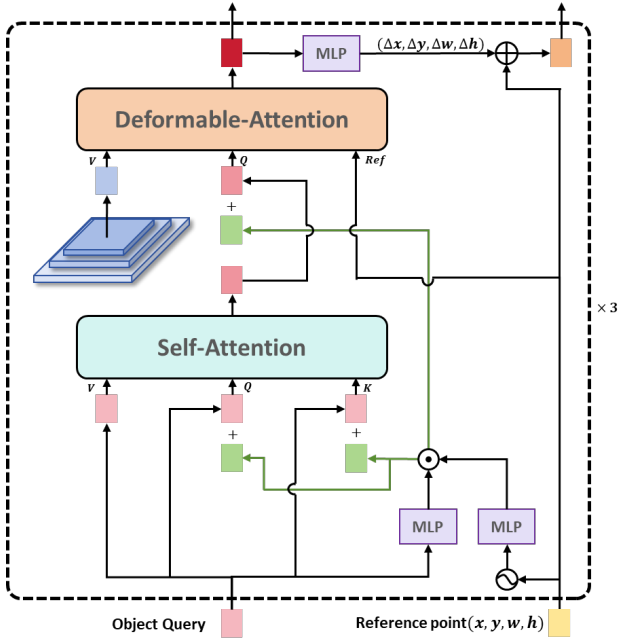


**Figure 5:** Illustrates the GAPE strategy at decoder. The small green rectangles in the diagram denote the positional encodings we designed.

As illustrated in fig. 5, we denote  $B_q$  as the  $q$ -th reference box,  $O_q$  as the  $q$ -th content query, and  $P_q$  as the  $q$ -th positional query, where  $D$  represents the dimension of Object Queries. Given reference box  $B_q(x_q, y_q, w_q, h_q)$  and content query  $O_q$ , the generation process of positional query  $P_q$  is formulated as:

$$\begin{aligned} PE(B_q) &= PE(x_q, y_q, w_q, h_q) \\ &= \text{Cat}(PE(x_q), PE(y_q), PE(w_q), PE(h_q)) \end{aligned} \quad (13)$$

$$P_q = \text{MLP}(O_q) \times \text{MLP}(PE(B_q)) \quad (14)$$

where  $PE$  denotes sinusoidal positional encoding, and  $Cat$  represents channel-wise concatenation. The positional encoding function maps floating-point numbers to  $D/2$  dimensional vectors, which are concatenated to form a  $2D$  dimensional vector and subsequently transformed to  $D$  dimensional positional embeddings through MLP operations. The MLP comprises two sub-modules, each consisting of a linear layer followed by ReLU activation, with feature dimension reduction performed in the first sub-module. To recalibrate the scale of positional embeddings, we train an additional MLP to generate scaling vectors conditioned on content information  $O_q$ , which are then applied through element-wise multiplication with the positional embeddings.

In the Self-Attention module, Queries and Keys incorporate positional terms, while Values contain only content information:

$$\text{Self-Attn} : Q_q = O_q + P_q$$

Stage	1	2	1&2
TP F Rate (%)	19.87	18.95	33.84
FP E Rate (%)	53.67	54.58	71.84

**Table 1**  
TP/FP Rate Analysis of RT-DETR-18's Stage 3 with Single and Combined Layers at IoU > 0.5

$$\begin{aligned} K_q &= O_q + P_q \\ V_q &= O_q \end{aligned} \quad (15)$$

In the Cross-Attention module, Queries are the updated  $O_q$  from the current decoder layer's Self-Attention output, Keys are directly derived from reference boxes  $B_q$ , and Values are obtained through sampling operations on multi-scale feature maps from the Efficient Hybrid Encoder output:

$$\begin{aligned} \text{Cross-Attn} : Q_q &= O_q + P_q \\ V &= \text{Sampling}(S) \end{aligned} \quad (16)$$

where  $S$  represents the multi-scale feature maps output by the Efficient Hybrid Encoder. The Sampling operation generates offset points through linear mapping of Queries via deformable attention mechanisms, adds them to reference points to obtain sampling points, and finally extracts corresponding values from feature maps  $S$  to derive  $V$ . This approach enables the reference points in the decoder's deformable attention to concentrate more effectively on objects and enhances the attention weights of reference points on objects (as demonstrated in Figure 6), thereby improving the model's localization capability for small objects and dense targets.

### 3.4. Selective Query Recollection

The VisDrone dataset is characterized by dense small objects and complex backgrounds, presenting a critical challenge in multi-stage decoding processes: later stages tend to diminish the confidence of correct predictions from earlier stages while simultaneously exacerbating erroneous predictions. Ideally, final-stage predictions should outperform those from earlier stages, as model evaluation is based on the ultimate prediction results. As illustrated in the visualization results of fig. 7: in the first column, the truck confidence decreases from 0.62 in Stage 1 to 0.06 in Stage 2, resulting in excessively low confidence in Stage 3; in the third column, Stage 1 correctly predicts a truck, but Stage 2 erroneously predicts it as a van, causing the error to be amplified in Stage 3.

This phenomenon stems from two fundamental causes: 1) the cascaded structure of decoders necessitates that stage-optimized queries (regardless of their positive or negative effects) propagate to downstream stages; 2) later stages lack sufficient supervision, where early-stage errors can be corrected by subsequent stages, but later stages exert more decisive influence on final predictions.

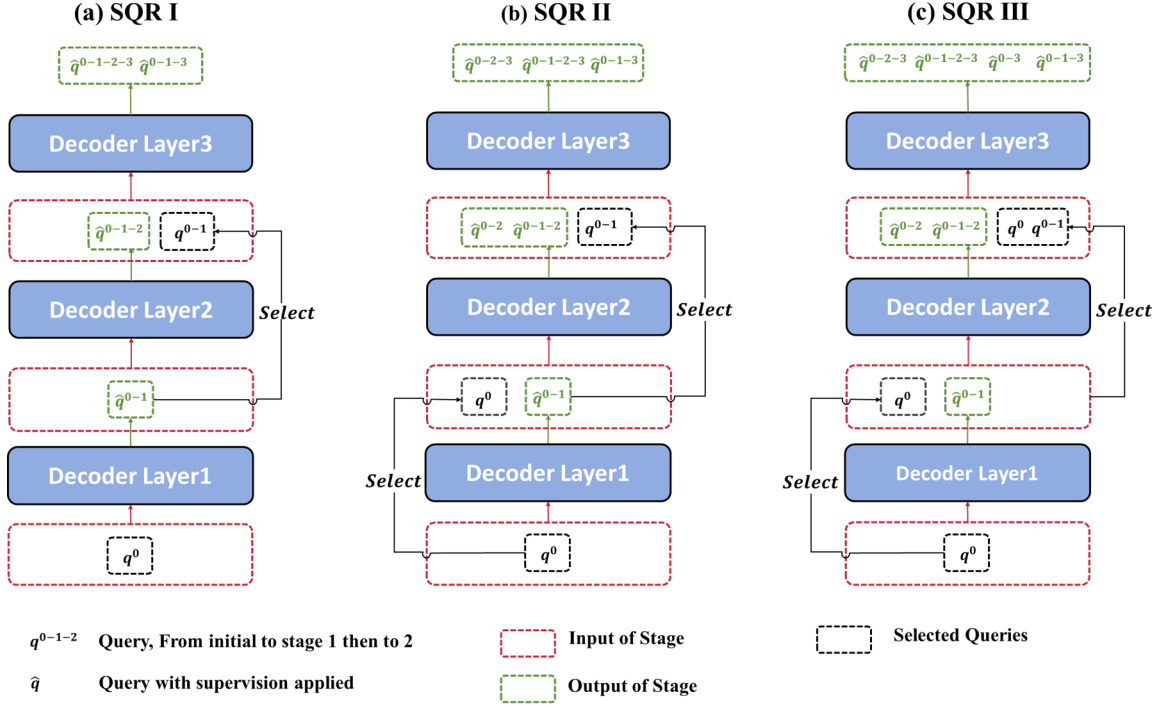


Figure 6: Illustration of the three variants of our SQR.

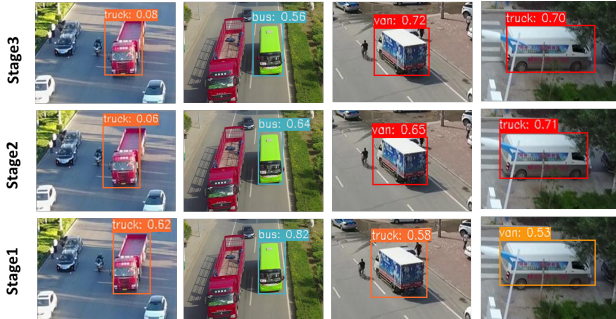


Figure 7: Visualizes RT-DETR-R18 predictions across stages (bottom→top: early→late). The first two columns highlight confidence drops on initially correct detections; the last two show early correct classifications turning into errors later (red boxes).

To quantify this phenomenon, we employ the True Positive Fading Rate (TP F Rate) [3] and False Positive Exacerbation Rate (FP E Rate) [3] metrics. Table 1 demonstrates that Stage 3 exhibits comparable TP F Rate and FP E Rate with individual Stage 1 and Stage 2, indicating that both stages contribute equally to this phenomenon. When Stage 3 is compared with the joint Stage 1+Stage 2, the TP F Rate reaches 33.84% and FP E Rate reaches 71.84%, confirming the prevalence of this phenomenon in small object detection scenarios with complex backgrounds.

To address this issue, as shown in fig. 6 we design three Selective Query Recollection (SQR) methods. Let  $D^j$  denote the  $j$ -th decoder mapping. For any finite index sequence  $\{k_1, k_2, \dots, k_m\}$ , we define:

$$q^{(0-k_1-k_2-\dots-k_m)} := D^{k_m} (D^{k_{m-1}} (\dots D^{k_1} (q^0) \dots)) \quad (17)$$

where  $q^0$  represents the initial state. The query  $q$  encompasses both object queries and reference points.

**SQR I:** Only introduces the input of  $D^2$  into the input of  $D^3$ . As the final layer of RT-DETR-R18, we hypothesize that providing additional supervision solely to  $D^3$  can mitigate cascading errors while reducing computational costs:

$$\begin{aligned} C^1 &= \{q^0\} \\ C^2 &= D^1(C^1) = \{q^{0-1}\} \\ C^3 &= D^2(C^2) \cup C^2 = \{q^{0-1-2}, q^{0-1}\} \end{aligned} \quad (18)$$

where  $C^j$  represents the input to the  $j$ -th decoder layer, and the output of  $D^j$  serves as the supervision signal for the  $j$ -th layer.

**SQR II:** Building upon SQR I, this method introduces the input of  $D^2$  into the input of  $D^3$ , thereby increasing the supervision quantity for both  $D^2$  and  $D^3$ . We hypothesize that  $q^0$  selected through Uncertainty-minimal Query Selection [33] may also possess the capability to correctly predict target boxes, potentially further alleviating cascading errors:

$$\begin{aligned} C^1 &= \{q^0\} \\ C^2 &= D^1(C^1) \cup C^1 = \{q^{0-1}, q^0\} \\ C^3 &= D^2(C^2) \cup D^1(C^1) = \{q^{0-1-2}, q^{0-2}, q^{0-1}\} \end{aligned} \quad (19)$$

**SQR III** Extending SQR II by introducing the input of  $D^1$  into the input of  $D^3$ , further augmenting the supervision quantity for  $D^3$ . Given that  $D^3$  plays a decisive role in prediction results, enhancing its supervision enables better optimization:

$$\begin{aligned} C^1 &= \{q^0\} \\ C^2 &= D^1(C^1) \cup C^1 = \{q^{0-1}, q^0\} \\ C^3 &= D^2(C^2) \cup C^2 = \{q^{0-1-2}, q^{0-2}, q^{0-1}, q^0\} \end{aligned} \quad (20)$$

Experimental validation demonstrates that SQR II outperforms other approaches across all metrics; therefore, SQR in subsequent sections specifically refers to this method. The experiments confirm that the SQR method effectively reduces both TPF Rate and FPE Rate, stabilizing the progressive optimization process of bounding boxes.

## 4. Experiment

### 4.1. Dataset and Experiment Setup

**Dataset:** In the domain of object detection in drone-captured aerial imagery, a crucial and widely adopted dataset is the VisDrone dataset [35]. This dataset is partitioned into three subsets with a ratio of 7:2:1, comprising a training set (6471 images), a validation set (548 images), and a test set (1610 images). The images within this dataset possess a maximum resolution of  $2000 \times 1500$  pixels and encompass 10 distinct object categories, including pedestrians, various vehicle types, bicycles, and motorcycles, thereby providing a comprehensive benchmark platform for the training and evaluation of object detection algorithms.

**Implementation Details:** The experiments were conducted on a high-performance computing server equipped with an NVIDIA GeForce RTX 8000 GPU, operating on the Ubuntu 20.04 operating system. The deep learning framework utilized was PyTorch 2.5.0, accelerated with CUDA 12.2. We employed the Adam optimizer with an initial learning rate of  $1 \times 10^{-4}$  and a weight decay of 0.0001 to mitigate overfitting. The model was trained for a total of 300 epochs with a batch size of 16, processing input images at a resolution of  $640 \times 640$ . Momentum was set to 0.9 to expedite convergence during the optimization process. For comprehensive evaluation, we adopted the evaluation metrics from the COCO dataset, including Average Precision (AP) with Intersection over Union (IoU) thresholds ranging from 0.5 to 0.95 in increments of 0.05, as well as AP at different scales[15].

### 4.2. Comparative Experiment

To systematically evaluate detection performance on the VisDrone benchmark, this study conducts a comparative analysis of three mainstream detection paradigms: conventional convolutional detectors, the YOLO series, and Transformer-based architectures (DETR). With the exception of traditional detectors, which utilized ImageNet pre-trained weights, all other models were trained from random

initialization to ensure a fair comparison under equivalent training conditions.

As delineated in Table 2, conventional convolutional detectors (Faster R-CNN, Cascade R-CNN, ATSS, TOOD) generally exhibited suboptimal performance on the VisDrone dataset. The best-performing among them, TOOD, achieved an  $AP_{50}$  of only 33.9%. This underperformance is primarily attributed to their anchor-box dependency mechanisms and multi-stage processing pipelines, which struggle to effectively address the high-density small objects and complex occlusions prevalent in aerial imagery. Notably, the limited transferability of pre-training strategies to the aerial domain further underscores the inherent bottlenecks of these traditional architectures.

The YOLO series of detectors demonstrated significant advantages in computational efficiency; for instance, YOLOv10m required only 58.9 GFLOPS and comprised 15.32M parameters. However, their  $AP_{50}$  (ranging from 19.0% to 19.8%) and small object  $AP_S$  (ranging from 8.7% to 9.6%) were considerably inferior to those of DETR-based architectures, reflecting the intrinsic limitations of anchor-based paradigms in multi-scale detection tasks. It is noteworthy that the architectural homogeneity across successive YOLO iterations (v8-v12) resulted in marginal performance enhancements, thereby corroborating the principle of diminishing returns from incremental improvements.

In the comparison of DETR-based architectures, HEDS-DETR achieved a 4.4 percentage point increase in  $AP_{50}$  and a 3.2 percentage point gain in  $AP_{50-90}$  relative to the baseline model RT-DETR-R18, while maintaining comparable computational costs (64.9 vs. 57.0 GFLOPS). Of particular significance, despite a 16% reduction in parameter scale compared to DEIM, our model surpassed the current state-of-the-art DETR variants, DFINE and DEIM, by 3.2% and 1.2% in  $AP_{50}$ , respectively. Furthermore, on critical small object detection metrics, our model demonstrated a +2.1%  $AP_S$  improvement over DEIM, further validating its competitive advantage in scenarios characterized by dense small objects and complex backgrounds.

### 4.3. Ablation Studies

Ablation studies were conducted on the VisDrone validation set to evaluate the contributions of individual components within the HEDS-DETR framework to detection accuracy. The detailed experimental results are presented in Table 3. The Frames Per Second (FPS) metric was benchmarked on a single NVIDIA RTX 3090 GPU.

The baseline model, RT-DETR-R18, devoid of any integrated innovative components, achieved a modest 42.9%  $AP_{50}$  and 17.6%  $AP_S$ , thereby underscoring the inherent technical challenges associated with small object detection in Unmanned Aerial Vehicle (UAV) imagery. This baseline model comprises 19.88M parameters and achieves a real-time inference speed of 172.4 FPS with a computational complexity of 57.0 GFLOPS.

By employing HFESNet as a substitute for the standard backbone network,  $AP_{50}$  was significantly improved by 2.8

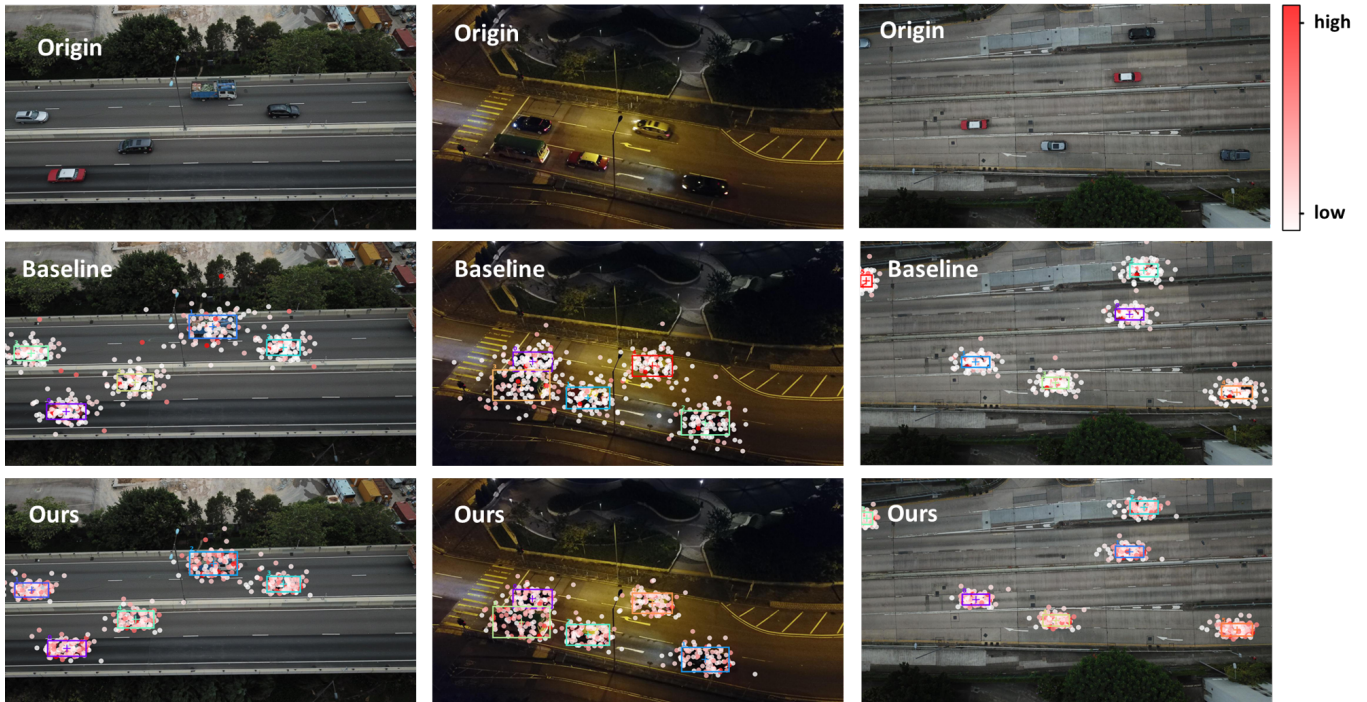


**Figure 8:** Visualization of deformable attention in the decoder. Reference points are marked with a cross, and each sampling point is shown as a solid circle; redder colors indicate higher attention weights.

**Table 2**  
Comparative Experiments on VisDrone-2019 Testset Benchmark

Model	AP <sub>50</sub> (%)	AP <sub>50-90</sub> (%)	AP <sub>s</sub> (%)	AP <sub>m</sub> (%)	GFLOPS	Params (M)
<b>Traditional Detectors</b>						
Faster-RCNN [21]	32.9	19.4	9.5	30.9	208	41.39
Cascade-RCNN [1]	32.6	19.4	9.9	30.9	236	69.29
ATSS [31]	33.8	20.4	10.0	31.7	110	38.91
TOOD [6]	33.9	20.4	10.2	31.7	199	32.04
<b>YOLO Series Detectors</b>						
YOLOv8m [12]	33.2	19.0	8.9	29.5	79.3	25.90
YOLOv9m [29]	33.8	19.4	9.3	30.3	77.9	20.22
YOLOv10m [27]	33.1	19.0	8.7	29.2	58.9	<b>15.32</b>
YOLOv11m [13]	34.4	19.8	9.6	30.3	68.5	20.11
YOLOv12m [25]	33.5	19.2	9.3	29.6	60.4	19.67
<b>DETR Series Detectors</b>						
RT-DETR-R18 [33]	33.8	19.1	10.6	28.2	57.0	19.88
DFINE [20]	35.0	20.0	10.9	29.0	<b>56.4</b>	19.19
DEIM [10]	37.0	21.2	12.4	30.6	<b>56.4</b>	19.19
HEGS-DETR (ours)	<b>38.2</b>	<b>22.3</b>	<b>12.7</b>	<b>32.3</b>	64.9	16.53

percentage points (45.7% vs. 42.9%). This demonstrates that enhancing deep semantic representations while preserving shallow-layer spatial details effectively improves the discriminability of small objects within complex backgrounds. Notably, the integration of HFESNet reduced computational costs by 7.7% (to 52.6 GFLOPS). Upon incorporating the ESOP strategy, AP<sub>50</sub> was further augmented to 46.2% (an additional 0.5% improvement). This module achieves optimized aggregation of small object features within a computational budget of 64.6 GFLOPS.

The introduction of the GAPE strategy yielded a 1.1% gain in AP<sub>50</sub>, reaching 47.3%. Its geometrically aware encoding effectively enhanced the discriminability of dense instances and the localization precision for small objects.

The SQR training strategy contributed a 0.7% improvement in AP<sub>50</sub> without incurring additional computational overhead, validating the positive impact of reinforcing supervision in later stages and alleviating decoder cascading errors for the detection of dense small objects. The complete HEGS-DETR model, while preserving the real-time

**Table 3**  
Ablation Study on Architectural Components of HEDS-DETR.

HFESNet	ESOP	GAPE	SQR	AP <sub>50</sub> (%)	AP <sub>50-90</sub> (%)	AP <sub>s</sub> (%)	GFLOPS	Params (M)	FPS
–	–	–	–	42.9	25.6	17.6	57.0	19.88	<b>172.4</b>
✓	–	–	–	45.7	27.6	19.4	<b>52.6</b>	<b>15.42</b>	158.7
✓	✓	–	–	46.2	28.0	19.9	64.6	16.30	135.1
✓	✓	✓	–	47.3	28.6	20.7	64.9	16.53	131.6
✓	✓	✓	✓	<b>48.0</b>	<b>29.4</b>	<b>20.9</b>	64.9	16.53	131.6

**Table 4**  
Comparison of Different ESOP Variants on VisDrone Validation Set.

Variant	Average Precision				GFLOPS	Params (M)
	AP <sub>50</sub> (%)	AP <sub>50-90</sub> (%)	AP <sub>s</sub> (%)	AP <sub>m</sub> (%)		
ESOP	<b>44.6</b>	<b>26.7</b>	<b>18.3</b>	<b>37.0</b>	65.2	20.50
ESOP-Conv	43.7	26.0	18.2	35.3	59.7	20.05
ESOP-NP	43.1	25.5	18.1	34.7	62.4	20.28
RT-DETR-R18	42.9	25.6	17.6	35.4	<b>57.0</b>	<b>19.88</b>

performance characteristic of RT-DETR-R18 (131.6 FPS), elevated the AP<sub>50</sub> by 5.1 percentage points to 48.0%.

Collectively, these experimental results demonstrate that the enhancement strategies proposed herein significantly bolster the model’s representation learning capabilities for small object detection tasks.

#### 4.4. Comparative Analysis of Different ESOP Schemes

To validate the efficacy of the critical components within our proposed ESOP strategy, we conducted ablation studies comparing three variants against the baseline model, RT-DETR-R18. Table 4 systematically evaluates the performance of each model.

Our ESOP architecture surpasses the two modified variants and the baseline RT-DETR-R18 model across all AP metrics. Specifically, it achieves 44.6% in AP<sub>50</sub> and 18.3% in small object accuracy (AP<sub>s</sub>), representing improvements of 1.7% and 0.7% respectively, over the baseline model.

The ESOP-Conv variant, wherein the SpdConv in S2 processing is replaced with a conventional strided convolution, exhibits a significant performance degradation (a 0.9% decrease in AP<sub>50</sub> and a 1.7% reduction in AP<sub>M</sub>). This substantiates our hypothesis that standard convolutional operations, when downsampling high-resolution feature maps, inadequately preserve the fine-grained spatial information crucial for detecting small objects.

The ESOP-NP variant, which removes the COKBlock pre-fusion module, incurs a notable performance loss despite a comparable computational cost (62.4 GFLOPS vs. 65.2 GFLOPS), particularly in the detection of medium-sized objects (AP<sub>M</sub> of 34.7% vs. 37.0%). This highlights that without the COKBlock pre-fusion, employing only RepBlock for feature fusion renders it challenging for the model

to effectively integrate cross-scale features with significant semantic disparities.

It is noteworthy that although the baseline RT-DETR-R18 incurs the lowest computational cost (57.0 GFLOPS), its performance significantly trails all ESOP variants, especially in small object detection (AP<sub>s</sub> of 17.6% vs. 18.3%). This performance gap validates our architectural enhancements: through the strategic integration of shallow features and optimized fusion mechanisms, a substantial improvement in detection capability is achieved with only a modest increase in computational load (+8.2 GFLOPS) and parameter count (+0.62M).

#### 4.5. SQR Validation Experiments

We first compare three variants of the SQR strategy proposed in section 3.4. SQR-Baseline is based on RT-DETR-R18, incorporating the HEFSNet backbone, ESOP strategy, and GAPE method.

As shown in Table 5, SQR-Baseline achieves an AP<sub>50</sub> metric of 47.3%, with small object precision (AP<sub>s</sub>) at 20.7%. SQR I maintains AP<sub>50</sub> and AP at 47.3% and 28.6%, respectively, indicating that merely increasing supervision in  $D^3$  is insufficient to mitigate the decoder’s cascading errors.

SQR II raises AP<sub>50</sub> to 48.0% (+0.7%), AP to 29.4% (+0.8%), and small- and medium-object AP<sub>s</sub> to 20.9% and 40.2%, respectively. This improvement is achieved by incrementally increasing the number of supervision layers within the decoder, which alleviates cascading errors and stabilizes bounding-box optimization. Although training time increases by 34%, this efficiency–accuracy trade-off is acceptable given the significant precision gains; moreover, it incurs no additional inference time or model complexity.

**Table 5**

Comparison of Different SQR Variants VisDrone Validation Set.

Model	Average Precision				Train Time	Loss Queries (D <sup>2</sup> )	Loss Queries (D <sup>3</sup> )
	AP <sub>50</sub> (%)	AP <sub>50-90</sub> (%)	AP <sub>s</sub> (%)	AP <sub>m</sub> (%)			
SQR-Baseline	47.3	28.6	20.7	38.6	1.00×	1	1
SQR I	47.3	28.6	20.6	39.1	1.06×	1	2
SQR II	<b>48.0</b>	<b>29.4</b>	<b>20.9</b>	<b>40.2</b>	1.34×	2	3
SQR III	47.4	28.6	20.6	39.2	1.40×	2	4

Model	TP Threshold	TP F Rate (%)	FP E Rate (%)
SQR-Baseline	IoU > 0.25	31.91	72.40
SQR II	IoU > 0.25	<b>30.79</b>	<b>69.42</b>
SQR-Baseline	IoU > 0.50	32.26	72.38
SQR II	IoU > 0.50	<b>28.35</b>	<b>69.21</b>
SQR-Baseline	IoU > 0.75	27.57	72.32
SQR II	IoU > 0.75	<b>22.36</b>	<b>69.44</b>

**Table 6**

Comparative Analysis of Localization Stability Under Varying IoU Thresholds.

SQR III raises AP<sub>50</sub> to 47.4% (+0.1%) but increases training cost by 40%. This limited gain stems from introducing q0 into the D3 input, which creates a significant learning gap—additional noise that outweighs any potential benefits.

As depicted in Table 6, we quantitatively evaluated bounding box stability under varying localization requirements. Our SQR strategy consistently demonstrates significant improvements in both True Positive (TP) fading rate (TP F Rate) and False Positive (FP) exacerbation rate (FP E Rate) across all evaluation conditions. First, at a baseline IoU threshold of 0.25, SQR II reduced the TP F Rate by 1.12% (from 31.91% to 30.79%). Second, the improvements became more pronounced at higher precision thresholds. When IoU > 0.5, the TP F Rate saw a relative reduction of 3.91% (from 32.26% to 28.35%). Notably, under the strict IoU threshold of 0.75, which demands precise bounding box localization, SQR II achieved a 5.21% decrease in TP F Rate (27.57% → 22.36%). This trend of increasing improvement with higher IoU thresholds (also observed for the FP E Rate) suggests that our training strategy effectively mitigates cascading errors in the decoder, particularly those occurring at high IoU thresholds.

#### 4.6. Visualization

To gain deeper insight into how our proposed SQR strategy and GAPE strategy enhance object localization performance, we visualize the sampling behavior of the deformable cross-attention in the final decoder layer.

To recall, for a given object query  $q$ , the deformable cross-attention mechanism first generates two distinct sets of outputs via independent linear projections. One projection predicts the sampling offsets  $\{\Delta p_m\}_{m=1}^M$  for  $M$  points, while the other predicts their corresponding attention weights

$\{a_m\}_{m=1}^M$ . Each sampling point  $p_m$  is computed by adding the learned offset  $\Delta p_m$  to the query's reference point  $Ref$ , such that  $p_m = Ref + \Delta p_m$ . We visualize both  $p_m$  and  $a_m$ .

In fig. 8, the reference point for each object query is denoted by a cross, and the corresponding sampling points are represented by colored dots, where the color intensity is proportional to the attention weight  $a_m$ . Compared to the baseline RT-DETR-R18 (middle row), our model, HEGS-DETR (bottom row), exhibits a significantly more pronounced sampling focus. The sampling points are densely aggregated within the foreground regions of the predicted bounding boxes, and the attention weights within each box are substantially enhanced, as indicated by the deeper red hues. This phenomenon demonstrates that our deformable attention mechanism effectively learns to concentrate sampling resources on the most information-rich spatial regions, thereby enabling sharper object boundary delineation and achieving more precise localization capabilities.

To analyze the advantages of our model, which incorporates the HEGSNet backbone, over the baseline RT-DETR-r18, we conduct a visual analysis of the attention maps from the Intra-scale Feature Interaction (AIFI) module. This process begins with the raw self-attention weight matrix, denoted as  $\mathbf{A} \in \mathbb{R}^{N_h \times (H \times W) \times (H \times W)}$ , where  $N_h$  is the number of attention heads and  $H \times W$  represents the spatial resolution of the flattened feature map.

To generate a single, interpretable saliency map, we employ a two-stage aggregation strategy. The first stage involves averaging across all  $N_h$  attention heads. In the second stage, we calculate the mean attention received by each spatial token from all other tokens, a procedure that effectively compresses the query dimension. This process yields a vector quantifying the importance of each token. The final attention map,  $\mathbf{M}_{attn}$ , is formally defined as:

$$\mathbf{M}_{attn} = \text{Reshape}_{H,W} \left( \text{mean}_j \left( \frac{1}{N_h} \sum_{i=1}^{N_h} \mathbf{A}_{j,k}^{(i)} \right) \right) \quad (21)$$

where  $\mathbf{A}_{j,k}^{(i)}$  is the attention weight from query token  $j$  to key token  $k$  in the  $i$ -th head,  $\text{mean}_j(\cdot)$  denotes the averaging operation over the query dimension, and  $\text{Reshape}_{H,W}(\cdot)$  transforms the resulting  $1 \times (H \times W)$  importance vector into an  $H \times W$  dimensional map.

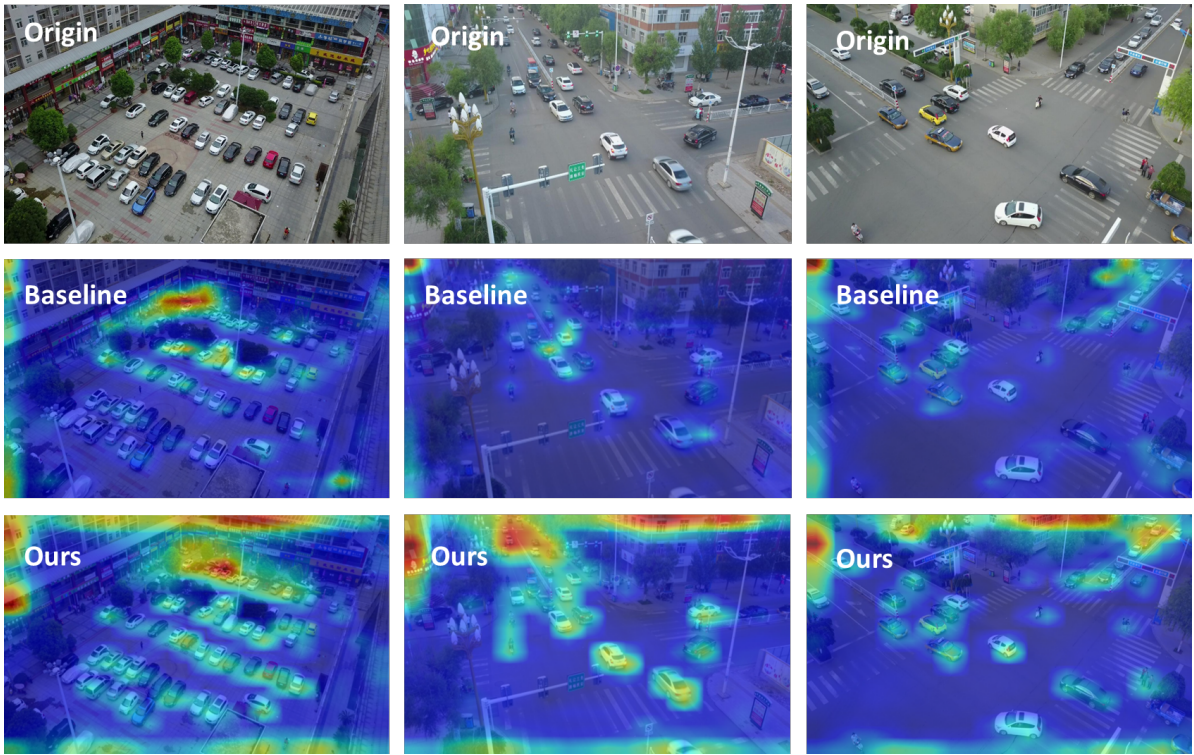


Figure 9: Visualization of the attention maps in the AIFI [33] module.

By overlaying this attention map  $M_{attn}$  onto the original image, we can intuitively observe the model’s attentional focus. As depicted in Figure 1, the attention maps generated by our model indicate that HEGS-DETR more effectively focuses on densely packed small objects and their surrounding contextual information compared to the RT-DETR-r18 baseline. This result substantiates that our proposed HEGSNet architecture enhances the discriminative power of the final feature maps, which is crucial for subsequent object localization and foreground-background separation.

## 5. Conclusion

This paper systematically addresses the long-standing trade-off between accuracy and real-time performance in aerial object detection, particularly in complex scenarios characterized by small object scales, high density, and occlusions. We propose a holistic and synergistic solution based on RT-DETR that comprehensively enhances feature representation and localization precision without compromising efficiency.

The core contribution of this research lies in the synergy of multi-dimensional architectural innovations. First, we propose the High-Frequency Enhanced Semantics Network (HFESNet), a novel backbone that synergistically optimizes spatial detail preservation and semantic context extraction. This design enhances high-level semantic expression while

preserving fine-grained spatial features, significantly improving the discriminative power of object features in complex aerial scenes. To address the information degradation problem inherent in small object detection, we design the Efficient Small Object Pyramid (ESOP), a lightweight feature pyramid module that innovatively integrates high-resolution  $S_2$  feature layers to substantially boost the recall of small objects at a minimal computational cost. Furthermore, we enhance the decoder’s performance in dense scenes via a dual mechanism: the Selective Query Recollection (SQR) training strategy, which achieves more stable bounding box regression by mitigating error accumulation, and the Geometry-aware Position Encoding (GAPE) module, which introduces explicit spatial priors to markedly improve localization precision in densely packed scenarios.

Overall, extensive experiments on the challenging VisDrone dataset validate the superiority of our method. Compared to the RT-DETR baseline, our model achieves a 5.1 percentage point improvement in  $AP_{50}$  and a 3.8 percentage point improvement in AP, all while reducing the parameter count by 4 million and maintaining real-time performance. Future work will focus on extending these architectural concepts to related aerial analysis tasks, including object tracking and semantic segmentation.

## 6. Acknowledgments

This research was supported by Natural Science Foundation of Guangdong Province (Grant No. 2025A1515011771)

and Guangzhou Science and Technology Plan Project (Grant No. 2023B01J0046, 2024E04J1242).

## 7. Data availability

Data will be made available on request.

## References

- [1] Cai, Z., Vasconcelos, N., 2018. Cascade r-cnn: Delving into high quality object detection, in: Proceedings of the IEEE conference on computer vision and pattern recognition, pp. 6154–6162.
- [2] Carion, N., Massa, F., Synnaeve, G., Usunier, N., Kirillov, A., Zagoruyko, S., 2020. End-to-end object detection with transformers, in: European conference on computer vision, Springer. pp. 213–229.
- [3] Chen, F., Zhang, H., Hu, K., Huang, Y.K., Zhu, C., Savvides, M., 2023. Enhanced training of query-based object detection via selective query recollection, in: Proceedings of the IEEE/CVF conference on computer vision and pattern recognition, pp. 23756–23765.
- [4] Cui, Y., Ren, W., Knoll, A., 2024. Omni-kernel network for image restoration, in: Proceedings of the AAAI conference on artificial intelligence, pp. 1426–1434.
- [5] Dai, T., Wang, J., Guo, H., Li, J., Wang, J., Zhu, Z., 2024. Freqformer: Frequency-aware transformer for lightweight image super-resolution, in: IJCAI.
- [6] Feng, C., Zhong, Y., Gao, Y., Scott, M.R., Huang, W., 2021. Tood: Task-aligned one-stage object detection, in: ICCV.
- [7] Gao, G., Wang, Y., Chen, Y., Yang, G., Yao, L., Zhang, X., Li, H., Li, G., 2024. An oriented ship detection method of remote sensing image with contextual global attention mechanism and lightweight task-specific context decoupling. *IEEE Transactions on Geoscience and Remote Sensing*.
- [8] He, B., Ji, X., Li, G., Cheng, B., 2024. Key technologies and applications of uavs in underground space: a review. *IEEE Transactions on Cognitive Communications and Networking* 10, 1026–1049.
- [9] Henn, K.A., Peduzzi, A., 2024. Surface heat monitoring with high-resolution uav thermal imaging: Assessing accuracy and applications in urban environments. *Remote Sensing* 16, 930.
- [10] Huang, S., Lu, Z., Cun, X., Yu, Y., Zhou, X., Shen, X., 2025. Deim: Detr with improved matching for fast convergence.
- [11] Huang, S., Ren, S., Wu, W., Liu, Q., 2024. Discriminative features enhancement for low-altitude uav object detection. *Pattern Recognition* 147, 110041.
- [12] Jocher, G., Chaurasia, A., Qiu, J., 2023. Ultralytics YOLO. URL: <https://github.com/ultralytics/ultralytics>.
- [13] Khanam, R., Hussain, M., 2024. Yolov11: An overview of the key architectural enhancements. URL: <https://arxiv.org/abs/2410.17725>, arXiv:2410.17725.
- [14] Lin, T.Y., Dollár, P., Girshick, R., He, K., Hariharan, B., Belongie, S., 2017. Feature pyramid networks for object detection, in: Proceedings of the IEEE conference on computer vision and pattern recognition, pp. 2117–2125.
- [15] Lin, T.Y., Maire, M., Belongie, S., Hays, J., Perona, P., Ramanan, D., Dollár, P., Zitnick, C.L., 2014. Microsoft coco: Common objects in context, in: Computer vision—ECCV 2014: 13th European conference, Zurich, Switzerland, September 6–12, 2014, proceedings, part v 13, Springer. pp. 740–755.
- [16] Liu, S., Qi, L., Qin, H., Shi, J., Jia, J., 2018. Path aggregation network for instance segmentation, in: Proceedings of the IEEE conference on computer vision and pattern recognition, pp. 8759–8768.
- [17] Liu, Y., Wang, T., Zhang, X., Sun, J., 2022. Petr: Position embedding transformation for multi-view 3d object detection, in: European conference on computer vision, Springer. pp. 531–548.
- [18] Meng, D., Chen, X., Fan, Z., Zeng, G., Li, H., Yuan, Y., Sun, L., Wang, J., 2021. Conditional detr for fast training convergence, in: Proceedings of the IEEE/CVF international conference on computer vision, pp. 3651–3660.
- [19] Peng, H., Xie, H., Liu, H., Guan, X., 2024a. Lgff-yolo: small object detection method of uav images based on efficient local–global feature fusion. *Journal of Real-Time Image Processing* 21, 167.
- [20] Peng, Y., Li, H., Wu, P., Zhang, Y., Sun, X., Wu, F., 2024b. D-fine: Redefine regression task in detrs as fine-grained distribution refinement. URL: <https://arxiv.org/abs/2410.13842>, arXiv:2410.13842.
- [21] Ren, S., He, K., Girshick, R., Sun, J., 2015. Faster R-CNN: Towards real-time object detection with region proposal networks. arXiv preprint arXiv:1506.01497.
- [22] Sunkara, R., Zhang, R., Jiang, Y., Kong, T., Xu, C., Zhan, W., Tomizuka, M., Li, L., Yuan, Z., Wang, C., et al., 2021. Sparse r-cnn: End-to-end object detection with learnable proposals, in: Proceedings of the IEEE/CVF conference on computer vision and pattern recognition, pp. 14454–14463.
- [23] Sunkara, R., Luo, T., 2022. No more strided convolutions or pooling: A new cnn building block for low-resolution images and small objects, in: Joint European conference on machine learning and knowledge discovery in databases, Springer. pp. 443–459.
- [24] Tan, M., Pang, R., Le, Q.V., 2020. Efficientdet: Scalable and efficient object detection, in: Proceedings of the IEEE/CVF conference on computer vision and pattern recognition, pp. 10781–10790.
- [25] Tian, Y., Ye, Q., Doermann, D., 2025. Yolov12: Attention-centric real-time object detectors. URL: <https://arxiv.org/abs/2502.12524>, arXiv:2502.12524.
- [26] Tong, K., Wu, Y., Zhou, F., 2020. Recent advances in small object detection based on deep learning: A review. *Image and Vision Computing* 97, 103910.
- [27] Wang, A., Chen, H., Liu, L., Chen, K., Lin, Z., Han, J., Ding, G., 2024a. Yolov10: Real-time end-to-end object detection. URL: <https://arxiv.org/abs/2405.14458>, arXiv:2405.14458.
- [28] Wang, C.Y., Liao, H.Y.M., Wu, Y.H., Chen, P.Y., Hsieh, J.W., Yeh, I.H., 2020. Cspnet: A new backbone that can enhance learning capability of cnn, in: Proceedings of the IEEE/CVF conference on computer vision and pattern recognition workshops, pp. 390–391.
- [29] Wang, C.Y., Yeh, I.H., Liao, H.Y.M., 2024b. Yolov9: Learning what you want to learn using programmable gradient information. URL: <https://arxiv.org/abs/2402.13616>, arXiv:2402.13616.
- [30] Wang, J., Du, P., Yang, S., Zhang, Z., Ning, J., 2024c. A spatial arrangement preservation based stitching method via geographic coordinates of uav for farmland remote sensing image. *IEEE Transactions on Geoscience and Remote Sensing*.
- [31] Zhang, S., Chi, C., Yao, Y., Lei, Z., Li, S.Z., 2020. Bridging the gap between anchor-based and anchor-free detection via adaptive training sample selection, in: CVPR.
- [32] Zhang, Z., Lu, X., Cao, G., Yang, Y., Jiao, L., Liu, F., 2021. Vit-yolo: Transformer-based yolo for object detection, in: Proceedings of the IEEE/CVF international conference on computer vision, pp. 2799–2808.
- [33] Zhao, Y., Lv, W., Xu, S., Wei, J., Wang, G., Dang, Q., Liu, Y., Chen, J., 2024. Detrs beat yolos on real-time object detection, in: Proceedings of the IEEE/CVF conference on computer vision and pattern recognition, pp. 16965–16974.
- [34] Zheng, H., Chang, Z., Li, Y., Zhu, J., Wang, W., Yang, Q., Xie, C., Zhang, J., Liu, J., 2024. An efficient and fast image mosaic approach for highway panoramic uav images. *IEEE Journal of Selected Topics in Applied Earth Observations and Remote Sensing*.
- [35] Zhu, P., Wen, L., Du, D., Bian, X., Fan, H., Hu, Q., Ling, H., 2021a. Detection and tracking meet drones challenge. *IEEE Transactions on Pattern Analysis and Machine Intelligence* 44, 7380–7399.
- [36] Zhu, X., Lyu, S., Wang, X., Zhao, Q., 2021b. Tph-yolov5: Improved yolov5 based on transformer prediction head for object detection on drone-captured scenarios, in: Proceedings of the IEEE/CVF international conference on computer vision, pp. 2778–2788.